Technische Universität München
Fakultät für Physik

Abschlussarbeit im Bachelorstudiengang Physik

Study of the $\pi^-\pi^+$ P-Wave Amplitude in the $\pi^-\pi^-\pi^+$ System Produced in Inelastic $\pi^- p$ Collision at COMPASS

Martin Bartl

November 25, 2019

Erstgutachter (Themensteller): Prof. Stephan Paul
Zweitgutachter: Prof. Bruno Leibundgut

Contents

Introduction

The field theory of the strong interaction is called quantum chromodynamics (QCD). It describes the interaction of quarks, which are the basic constituents of hadrons, via gluon exchange. In higher-energy reactions with a large momentum transfer, i.e. at distance scales much smaller than the typical size of a nucleon, the coupling constant α_s of the strong interaction becomes small and quarks behave as quasi-free particles. In this regime, one can use perturbation theory, i.e. a series expansion in powers of α_s, to obtain highly precise and verified predictions.
In contrast, at lower energies in the range of hadron masses, the coupling constant becomes large, rendering the standard perturbation-theory approach inapplicable. Therefore, understanding strong-force processes at low energy is one of the main open questions of the standard model. One way of obtaining more information about the interaction of quarks and gluons at low energies is to study the excitation spectrum of hadrons. Mesons are particularly interesting, because in the constituent quark model they are bound states of quark and antiquark and hence the simplest kind of hadrons. One example is the $\rho(770)$, the lightest meson decaying via the strong force nearly exclusively into two pions [1]. Typically, Breit-Wigner parameterizations are used to describe the amplitude of short-lived hadron resonances, which is a good approximation for a single isolated narrow resonance, but cannot be used to describe multiple resonances such as excited ρ states.
In this thesis we analyze data from the COMPASS experiment at CERN on $\pi^-\pi^-\pi^+$ events produced in inelastic scattering of a high-energy π^- beam of a proton target. Our goal is to extract for the first time ground-state as well as excited ρ resonances from the measured amplitude of the $\pi^-\pi^+$ P-wave subsystem in a $\pi^-\pi^-\pi^+$ system with $J^P = 1^+$ using a model amplitude that is an analytic function in the complex s-plane, where s is the $\pi^-\pi^+$ mass squared.
This thesis is organized as follows. In ch. 2, we introduce the partial-wave analysis method and outline an extension of this method called the freed-isobar method. In ch. 3 we introduce the theoretical model to describe the $\pi^-\pi^+$ P-wave amplitude, which was derived in ref. [2] and allows multiple resonances. This leads to the definition of pole parameters, which are process-independent properties corresponding to masses and widths of these resonances. The fit method used to optimize the model parameters is explained in ch. 4. It takes into account and resolves so-called zero-mode ambiguities. The results of the fits are presented in ch. 5. A summary and an outlook are given in ch. 6.

Chapter 1

The COMPASS Experiment

The analyzed data were taken by COMPASS (COmmon Muon Proton Apparatus for Structure and Spectroscopy), a fixed target experiment at CERN.

1.1 Experimental Setup

The COMPASS experiment has four main sections (fig. 1.1). First of all, the beam line for COMPASS is the M2 beam line of the CERN SPS accelerator, which for the data used here was tuned to deliver a secondary π^--beam with an energy of 190 GeV. This beam hits the liquid-hydrogen target. The produced and scattered hadrons are detected in two detector sections. Firstly, the large-angle spectrometer, around the SM1 dipole magnet, detects particles with up to 180 mrad polar angle with respect to the beam axis. Secondly, the small-angle spectrometer, from the SM2 dipole magnet on, detects particles with smaller angles. For the analyzed process (see sec. 1.2) it

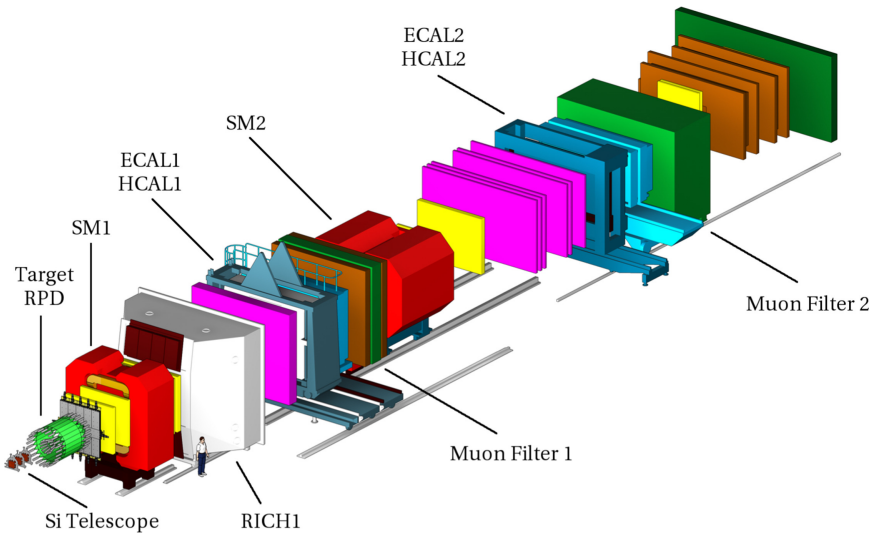

Figure 1.1: 3D view of the COMPASS experimental setup [3].

is important to precisely measure the momenta of the produced particles. For this task, the COMPASS spectrometer is equipped with several detectors that track the trajectories.
The direction of the beam particle is measured with high precision by a set of double-sided silicon microstrip detectors, which are located upstream of the target. Directly after the target a second set of silicon detectors measures the outgoing particles. The high spatial resolution of these detectors leads to high precision in the reconstruction of the position of the interaction point. In the two spectrometer stages, micro-pattern gaseous detectors, multi-wire proportional chambers and drift chambers are used to measure the trajectories of the forward-going particles. Both spectrometer stages are equipped with electromagnetic and hadronic calorimeters (ECAL and HCAL) for the identification of photons, electrons, and hadrons respectively.
For more detailed information see refs. [3, 4].

1.2 Analyzed Process

We analyze events of the inelastic scattering reaction

$$\pi^- p \to \pi^- \pi^+ \pi^- p, \tag{1.1}$$

which were selected from the COMPASS data [5, 6]. In this reaction, a negatively charged pion π^- scatters with a target proton p via the strong interaction (exchange of a pomeron $\mathbb{P}$). The pion is excited in a state with the mass $m_{3\pi}$, which decays via the strong interaction into three pions (fig. 1.2).
The kinematics of this process are characterized by $m_{3\pi}$ and the Mandelstam vari-

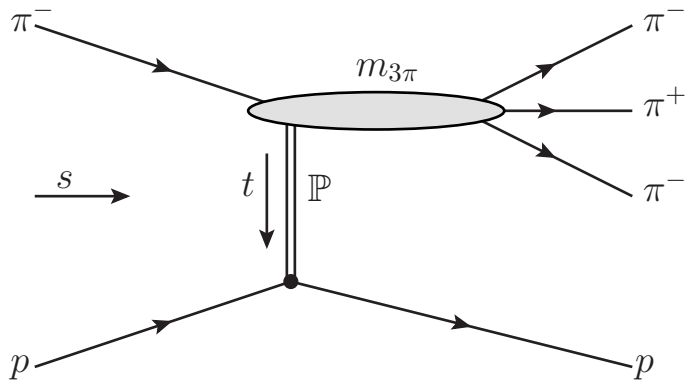

Figure 1.2: Diagram for the process $\pi^- p \to \pi^- \pi^+ \pi^- p$.

ables s and t, where s is the squared center-of-mass energy of the initially incoming $p\pi^-_{(beam)}$ system and t is the squared four-momentum transfer between p and π^-_{beam}. In addition, we have to take into account that a minimal squared four-momentum transfer $|t|_{\text{min}}$ is needed to excite the beam to an invariant mass of $m_{3\pi}$, i.e. to describe the process we use the reduced four-momentum transfer squared:

$$t' = |t| - |t|_{\text{min}} > 0. \tag{1.2}$$

Due to analyzed kinematic region of $0.1\,(\text{GeV}/c)^2 < t' < 1.0\,(\text{GeV}/c)^2$, $|t|_{\text{min}}$ is insignificant, so that $t' \approx |t|_{\text{min}}$. Since at COMPASS the beam energy is fixed, $\sqrt{s}$ is fixed to about 19 GeV.
The exclusive sample for the process $\pi^- p \to \pi^-\pi^+\pi^- p$, in the kinematic range $0.5\,\text{GeV}/c^2 < m_{3\pi} < 2.5\,\text{GeV}/c^2$ and $0.1\,(\text{GeV}/c)^2 < t' < 1.0\,(\text{GeV}/c)^2$, containing about $46 \cdot 10^6$ events, was selected by ref. [5]. For these events kinematic distributions are shown in fig. 1.3. The $m_{3\pi}$ spectrum features intermediate states of the three-pions system indicated by arrows, while the t' spectrum behaves approximate exponentially and the $m_{3\pi}$ spectrum features intermediate states of the three-pions system indicated by arrows.

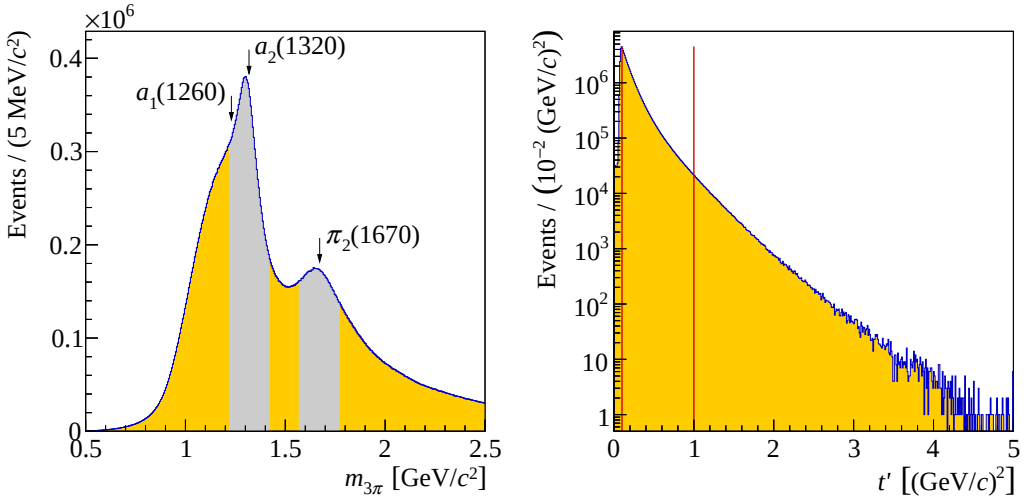

Figure 1.3: Kinematic distributions of the process $\pi^- p \to \pi^-\pi^+\pi^- p$. Left: the $m_{3\pi}$ spectrum. Right: the t' spectrum (taken from ref. [6]).

Chapter 2

Partial-Wave Analysis Model

Hadron resonances, which are composed of u, d or s quarks, decay via the strong interaction and have typical lifetimes of the order of 10^{-24}s. This means these resonances cannot be detected directly but be reconstructed from the daughter particles, that they decay into. Therefore, a partial-wave analysis is performed.

2.1 Particle Decays and the Isobar Model

Our analyzed process (see sec. 1.2) is a three-body decay of the form

$$X \to a + b + c. \tag{2.1}$$

Due to four-momentum conservation, the four-momenta of the particles in this process have to satisfy

$$P_X^\mu = \sum_{i=1}^{n} p_i^\mu, \tag{2.2}$$

with P_X^μ being the four-momentum of X and p_i^μ the four-momentum of the final-state particle i. Three-body decays can often be well approximated as a sequence of two-body decays, i.e. X decays first into an intermediate two-body state ξ, the so-called isobar, and one of the finale-state particles:

$$X \to \xi + c. \tag{2.3}$$

Then the isobar decays further into the two remaining finale-state particles

$$\xi \to a + b. \tag{2.4}$$

E.g. the decay $X^- \to \pi^-\pi^+\pi^-$ considered here can be decomposed into

$$X^- \to \xi^0 + \pi^-_{\text{Bachelor}} \quad \text{and} \quad \xi^0 \to \pi^- + \pi^+. \tag{2.5}$$

We consider only the $\pi^-\pi^+$ and not $\pi^-\pi^-$ state, due to the fact that the isobar is a meson, consisting of quark and anti-quark, and therefor cannot be twice negatively

charged. These two decays are part of the process $\pi^- p \to \pi^-\pi^+\pi^- p$, which was observed by COMPASS and can be decomposed into

$$\pi^- p \to X^- p, \quad X^- \to \xi^0 + \pi^-_{\text{Bachelor}} \quad \text{and} \quad \xi^0 \to \pi^- + \pi^+. \tag{2.6}$$

The kinematic distribution of the $\pi^-\pi^+$ state is shown in fig. 2.1, where we can see that the peaks of resonances are dominating the distribution, especially the peak of the $\rho(770)$ resonance.

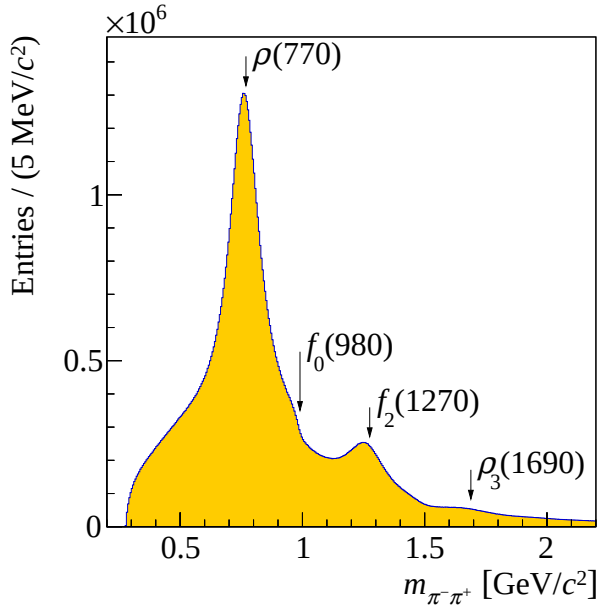

Figure 2.1: Kinematic distribution of the $\pi^-\pi^+$ state, in which four resonances are labeled. The picture is taken from ref. [6].

The diagram of the whole process is shown in fig. 2.2. X^- and ξ^0 have well-defined quantum numbers J^{PC}, where J is the spin, P and C are the eigenvalues of parity transformation and charge conjugation, respectively, M^ϵ characterizes the spin projection of X^- in a chosen basis, and L is the orbital angular momentum between ξ and the bachelor pion. These quantum numbers define the wave i, with $i = J^{PC}_X M^\epsilon J^{PC}_\xi L$.

2.2 Conventional Partial-Wave Analysis Method

The data contain contributions from various intermediate 3π states with different $J^{PC}M^\epsilon$ quantum numbers and various decay modes $\xi^0\pi^-$. In order to disentangle

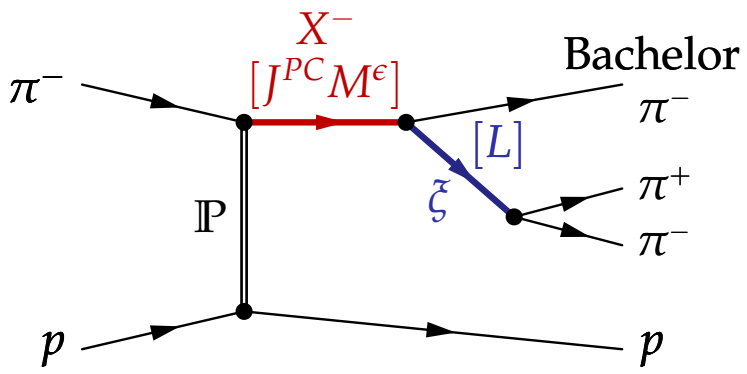

Figure 2.2: Diagram of the process $\pi^- p \to \pi^-\pi^+\pi^- p$ with intermediate state X^- and isobar ξ.

these contributions the PWA was performed.
For given values of $m_{3\pi}$ and t, the measured intensity distribution I, i.e. the number of measured counts as a function of the kinematic variables, is defined as

$$I(\boldsymbol{\tau}) = \left| \sum_i U_i(\boldsymbol{\tau}) \right|^2 . \tag{2.7}$$

I is a function of five phase-space variables that define the three-body kinematics and that are represented by $\boldsymbol{\tau}$, where $U_i(\boldsymbol{\tau})$ is the complex-valued amplitude for the process shown in fig. 2.2 of the wave i of a given wave set. We can define I like this, due to the model assumption that these amplitudes are fully coherent, which was confirmed as good in ref. [6]. With the assumption that X^- is a resonance and due to the independence of the propagation and decay of the resonance, we can factorize the amplitude so that every wave can be written as

$$U_i = T_i A_i(\boldsymbol{\tau}), \tag{2.8}$$

with $A_i(\boldsymbol{\tau})$ being the decay amplitude that describes the distribution of the final-state particles in the decay $X^- \to \pi^-\pi^+\pi^-$ for i and T_i being the transition amplitude that describes with which strength and phase the X^- is produced. Using the model for $I(\boldsymbol{\tau})$, we can write the joint probability density function for the measured data set $\mathbb{E}$ with N events, i.e. the extended likelihood function as function of the fit parameters $\boldsymbol{T} = \{T_i\}$ and $\mathbb{E}$:

$$L(\boldsymbol{T}; \mathbb{E}) = \frac{e^{\bar{N}} \bar{N}^N}{N!} \prod_{\text{event} \in \mathbb{E}} \frac{I(\boldsymbol{\tau}_{\text{event}})}{\bar{N}}, \tag{2.9}$$

where the first term in eq. (2.9) is a Poissonian factor describing the probability to measure N events, while expecting $\bar{N}$ events, and the second term defines the probability to measure $\mathbb{E}$, which is due to the independence of its events the product of the probabilities of each event in $\mathbb{E}$. The expected number of events $\bar{N}$, i.e. the normalization factor, is defined as:

$$\bar{N} = \int \mathrm{d}\boldsymbol{\tau} \rho_3(\boldsymbol{\tau}) \epsilon(\boldsymbol{\tau}) I(\boldsymbol{\tau}), \tag{2.10}$$

with $\rho_3(\boldsymbol{\tau})$ being the phase-space density and $\epsilon(\boldsymbol{\tau})$ being the total reconstruction efficiency of the detector, which can be determined with a Monte Carlo simulation. We use eq. (2.8) and can write eq. (2.10) after some calculation as:

$$\bar{N} = \sum_{i,j} T_i T_j^* \underbrace{\int \mathrm{d}\boldsymbol{\tau} \rho_3(\boldsymbol{\tau}) \epsilon(\boldsymbol{\tau}) A_i(\boldsymbol{\tau}) A_j^*(\boldsymbol{\tau})}_{\mathcal{I}_{i,j}}, \tag{2.11}$$

where the decay amplitudes $\{A_i\}$ are not allowed to contain any free parameters, because otherwise the calculation of $\bar{N}$ would become prohibitively expensive, and can be calculated using the isobar model. Consequentially $\mathcal{I}_{i,j}$ is independent of $\boldsymbol{T}$ and precalculable.
To fit the fit-parameters $\boldsymbol{T}$ to our data, i.e. to get the best possible description of the intensity, we maximize eq. (2.9) adjusting the production amplitudes. In order to calculate the decay amplitudes, we use again the factorization of propagation and decay as in sec. 2.1 and can write:

$$A_i(\boldsymbol{\tau}) = \mathcal{N}_i \Psi_i(\boldsymbol{\tau}) \Delta_i(m_{ab}), \tag{2.12}$$

where $\mathcal{N}_i$ is the real-valued constant that normalizes the amplitude and $\Psi_i(\boldsymbol{\tau})$ is the spin amplitude, which describes the angular distribution and is completely defined by the J^{PC} quantum numbers of X^- and ξ, M^ϵ of X^- and L. $\Delta_i(m_{ab})$ is the dynamic isobar amplitude describing the dependence of the decay amplitude on the mass $m_{ab} = m_\xi$ of the isobar, formed by the system (ab). With A_i being independent of $\boldsymbol{T}$, also $\Delta_i(m_\xi)$ has to be independent of $\boldsymbol{T}$. For this we use typical parameterizations of $\Delta_i(m_\xi)$, e.g. Breit-Wigner amplitudes or Flatté formulas [7], for which the parameters, i.e. mass and width of the isobar ξ, have to be taken from other measurements.

2.3 Freed-Isobar Partial-Wave Analysis Method

One of the main problems of the conventional PWA is the large systematic dependence on A_i, in particular on the chosen parameterizations and parameter values of

$\Delta_i(m)$. To solve these issues, a less model-dependent analysis technique, the so-called freed-isobar PWA [8, 9], was used. The basic idea of this approach is to replace the predefined fixed parameterizations of the dynamic isobar amplitudes by sets of indicator functions $\Delta^{\sqcap}_{\text{bin}}(m_\xi)$ such that

$$\Delta_i(m_\xi) = \sum_{\text{bin}}^{N_{\text{bins}}} \alpha_i^{\text{bin}} \Delta^{\sqcap}_{\text{bin,i}}(m_\xi), \text{ where } \Delta^{\sqcap}_{\text{bin}}(m_\xi) = \begin{cases} 1 \text{ if } m_\xi \in \text{bin}, \\ 0 \text{ otherwise.} \end{cases} \tag{2.13}$$

The sum runs over N_{bins} continuous m_ξ bins, which cover the whole kinematically allowed region. The dynamic amplitude is given by the complex-valued parameters α_i^{bin}, which are assumed to be constant within each m_ξ bin for the ith partial wave. Hence, using eqs. (2.8), (2.12) and (2.13), the total amplitude is

$$\begin{aligned} U(\boldsymbol{\tau}) &= \sum_i \mathcal{N}_i T_i \Psi_i(\boldsymbol{\tau}) \sum_{\text{bin}}^{N_{\text{bins}}} \alpha_i^{\text{bin}} \Delta^{\sqcap}_{\text{bin,i}}(m_\xi). \\ &= \sum_i \sum_{\text{bin}}^{N_{\text{bins}}} \mathcal{N}_i \underbrace{\mathcal{T}_i^{bin}}_{T_i \alpha_i^{\text{bin}}} \Delta^{\sqcap}_{\text{bin,i}}(m_\xi) \Psi_i(\boldsymbol{\tau}). \end{aligned} \tag{2.14}$$

This amplitude has the same structure as eq. (2.7), because of the replacements $\sum_i \to \sum_{\text{bin}}$ and $\mathcal{T}_i^{bin} \to T_i$, with $\mathcal{T}_i^{bin}$ being the new fit parameters. For a given $m_{3\pi}$ and t, $\mathcal{T}_i^{bin}$ leads to a binned approximation of the $m_{3\pi}$ dependence of $\Delta_i(m_\xi)$, which gives us information about the $\pi^-\pi^+$ subsystem with well-defined quantum numbers.

With the introduction of freed-isobar amplitudes in eq. (2.13) the PWA model has many more parameters. This causes continuous mathematical ambiguities for some combinations of partial waves, which we refer to as zero modes. These appear due to the fact that the two π^- in the analyzed final state are identical bosons. Hence, the decay amplitude obeys Bose symmetry, i.e. it is symmetric with respect to the exchange of the bachelor π^- and the π^- coming from the isobar. For some subsets S of partial waves, there is a freed-isobar amplitude $\Delta_i^0(m_\xi)$, for which the two terms from the Bose symmetrization in the decay amplitudes cancel each other for every point $\boldsymbol{\tau}$ in the phase space, i.e.

$$\sum_{i \in S} \Psi_i(\boldsymbol{\tau}) \Delta_i^0(m_\xi) + \text{Bose symm.} = 0. \tag{2.15}$$

Due to eq. (2.15) the corresponding decay amplitudes are invariant under shifts of the freed-isobar amplitudes of the form $\Delta_i \to \Delta_i + \mathscr{C}\Delta_i^0$, i.e.

$$\begin{aligned}\sum_{i\in S} A_i &= \sum_{i\in S} \Psi_i(\boldsymbol{\tau})\Delta_i(m_\xi) + \text{Bose symm.} \\ &= \sum_{i\in S} \Psi_i(\boldsymbol{\tau})[\Delta_i(m_\xi) + \mathscr{C}\Delta_i^0(m_\xi)] + \text{Bose symm.},\end{aligned} \tag{2.16}$$

where $\mathscr{C}$ is the complex-valued zero-mode coefficient. Therefore, also the total amplitude in eq. (2.14) and the intensity distribution in eq. (2.7) are invariant under these shifts of the freed-isobar amplitudes. This means that $\mathscr{C}$ cannot be determined from data so that

$$\Delta_i^{\text{meas}} = \Delta_i^{\text{phys}} + \mathscr{C}\Delta_i^0. \tag{2.17}$$

To determine $\mathscr{C}$ additional constraints are needed, e.g. a model for Δ_i^{phys}. Ref. [8] performed this required zero-mode correction i.a. for the $J_X^{PC} M^\epsilon J_\xi^{PC} L = 1^{++}0^+1^{--}S$ wave. Its results in fig. 2.3 show that due to the zero-modes the uncorrected result from the freed-isobar PWA (red) is shifted away from the dynamic amplitude used in the fixed-isobar PWA (grey), which can be assumed as a good approximation for the physically correct dynamic amplitude. For the further analysis the zero-modes are taken into account and are corrected with our model.

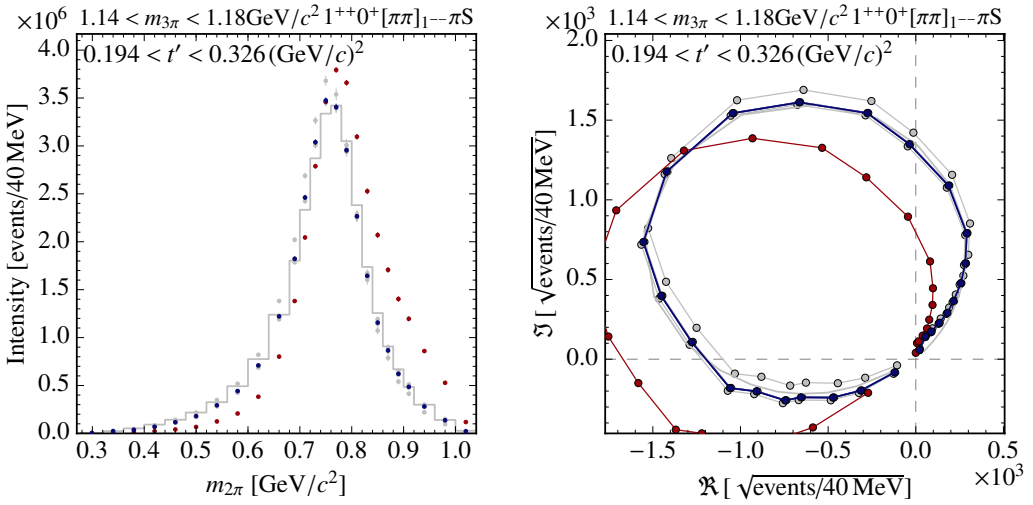

Figure 2.3: Intensity distribution and Argand diagram for the $J_X^{PC} M^\epsilon J_\xi^{PC} L = 1^{++}0^+1^{--}S$ wave before (red) and after (blue) resolving the zero-mode. The Argand diagram shows on the x-axis the real part of the dynamic amplitude and its imaginary part on the y-axis, while the dots represent points of equal spacing in $m_{2\pi}$.

Chapter 3

Theoretical Model for the $\pi^-\pi^+$ P-Wave Amplitude

3.1 The $\rho(770)$ and the Pion Vector Form Factor

Our goal is a description of the isobar amplitude with $J^{PC}_X M^\epsilon J^{PC}_\xi L = 1^{++}0^+1^{--}S$ in terms of resonances, where the ground state is the $\rho(770)$. Therefore, we use the parametrization from [2, 10], whose derivation we outline. Hence, we start with the pion form factor:

$$\langle \pi^+(p)\pi^-(p')|J^\mu|0\rangle = e(p-p')^\mu F(s), \tag{3.1}$$

where $\pi^+(p)$ and $\pi^-(p')$ are charged pion states with four-momentum p and p' respectively, $s = (p-p')^2$ is the center-of-mass energy of the $\pi^+\pi^-$ system squared, e is the elementary charge, J is the electromagnetic current, and $F(s) \equiv F_v(s)$ is the vector form factor. This form factor describes the production of two pions and can be expressed in terms of a source term M and a term describing the pion-pion interaction, i.e.

$$F(s) = M(s) + T(s)\Sigma(s)M(s), \tag{3.2}$$

with Σ being the self-energy and T being the T-matrix of a resonance, which can be written using the Lippmann-Schwinger equation:

$$T(s) = V(s) + V(s)\Sigma(s)T(s) \rightarrow T(s) = \frac{V(s)}{1 - V(s)\Sigma(s)}, \tag{3.3}$$

with V being the resonance potential. Inserting eq.(3.3) into eq.(3.2) we get:

$$F(s) = \frac{M(s)}{1 - V(s)\Sigma(s)}. \tag{3.4}$$

When considering a single resonance, the potential reads

$$V(s) = -\frac{m_\rho^2 g^2}{s - m_\rho^2}, \tag{3.5}$$

with m_ρ being the mass of the $\rho(770)$-resonance and $g \equiv g_{\pi\pi}$ its coupling to the two-pion final state. The source term can be parametrized as

$$M(s) = c - a \cdot V(s), \tag{3.6}$$

where c is a constant determined by the normalization of F (see eq. (3.20)) below, and a is the source-resonance coupling.
After inserting eqs.(3.5) and (3.6) into eq.(3.2), the form factor reads

$$F(s) = \frac{c\big(m_\rho^2 - s\big) - a m_\rho^2 g^2}{m_\rho^2 - s - m_\rho^2 g^2 \Sigma(s)}, \tag{3.7}$$

with m being the mass of the resonance.

3.2 Generalization of the Gounaris-Sakurai Parametrization

The next step is the generalization of the parametrization of the pion vector form factor developed by Gounaris and Sakurai [11]. Their ansatz was that the pion-pion scattering phase shift δ_1 in the P-wave satisfies the relation:

$$\frac{k^3(s)}{\sqrt{s}} \cot\delta_1 = k^2(s)h(s) + \alpha + \beta k^2(s), \tag{3.8}$$

with

$$k(s) = \sqrt{\frac{s}{4} - m_\pi^2}, \tag{3.9}$$

$$h(s) = \frac{2}{\pi}\frac{k(s)}{\sqrt{s}} \ln\left[\frac{\sqrt{s} + 2k(s)}{2m_\pi}\right]. \tag{3.10}$$

This effective-range Chew-Mandelstam equation is valid for a wide energy range. The form factor including the singularities and the correct phase reads

$$F(s) = \frac{f(0)}{f(s)}, \tag{3.11}$$

where

$$f(s) = \frac{k^3(s)}{\sqrt{s}} \cot\delta_1 - \mathrm{i}\frac{k^3(s)}{\sqrt{s}}. \tag{3.12}$$

The $\rho(770)$ parameters, i.e. mass m_ρ and width Γ_ρ, are defined via:

$$\cot\delta_1|_{s=m_\rho^2} = 0, \tag{3.13}$$

$$\left.\frac{\mathrm{d}\delta_1}{\mathrm{d}s}\right|_{s=m_\rho^2} = \frac{1}{m_\rho \Gamma_\rho}. \tag{3.14}$$

This leads to the form factor $F(s)$:

$$F(s) = \left(m_\rho^2 + d m_\rho \Gamma_\rho\right) \Big/ \left(\left(m_\rho^2 - s\right) + \Gamma_\rho \frac{m_\rho^2}{k^3(m_\rho^2)} \Big\{ k^2(s)\left[h(s) - h(m_\rho^2)\right] + k^2(m_\rho^2) h'(m_\rho^2)\left(m_\rho^2 - s\right) \Big\} - \mathrm{i} m_\rho \Gamma_\rho \left[\frac{k^3(s)}{k^3(m_\rho^2)}\right] \frac{m_\rho}{\sqrt{s}} \right) \tag{3.15}$$

with h' being the derivative of $h(s)$ and d being a constant defined via:

$$d = \frac{3}{\pi} \frac{m_\rho^2}{k^2(m_\rho^2)} \ln\left[\frac{m_\rho + 2k(m_\rho)}{2m_\rho}\right] + \frac{m_\rho}{2\pi k(m_\rho)} - \frac{m_\pi^2 m_\rho}{\pi k^3(m_\rho^2)}. \tag{3.16}$$

Comparing eqs.(3.7) and (3.15) yields the self energy

$$\Sigma(s) = \frac{1}{2\pi} \left\{ k^2(s)\left[h(m_\rho^2) - h(s)\right] - k^2(m_\rho^2)\, h'(m_\rho^2)\left(m_\rho^2 - s\right) + \mathrm{i} \frac{k^3(s)}{\sqrt{s}} \right\}. \tag{3.17}$$

3.3 Addition of Higher Excited ρ-Resonances

To construct an amplitude for multiple resonances, we have to extend the potential in eq.(3.5) to

$$V(s) = -\frac{m_1^2 g_1^2}{s - m_1^2} - \sum_{i=2} \frac{s g_i^2}{s - m_i^2}, \tag{3.18}$$

with m_i being the mass and g_i being the coupling of the ith resonance, i.e. $m_1 \equiv m_\rho$ and $g_1 \equiv g$. We define m_1 as real valued and other m_i as complex-valued. To reduce the influence of the higher resonances on the $\rho(770)$ ground state, which is already well described, m_i^2 was replaced by s in the numerators.
Also the source term in eq.(3.6) has to be adapted accordingly:

$$M(s) = c - a_1 \frac{m_1^2 g_1^2}{s - m_1^2} - \sum_{i=2} a_i \frac{s g_i^2}{s - m_i^2}. \tag{3.19}$$

The constant c is determined by the normalization of the form factor:

$$F(0) \stackrel{!}{=} 1 = \frac{c - a_1 g_1^2}{1 - V(0)\Sigma(0)} \rightarrow c = 1 - g_1^2\left[a_1 + \Sigma(0)\right]. \tag{3.20}$$

Inserting eqs.(3.17), (3.18) and (3.19) in eq.(3.4), the final pion vector form factor for n ρ-resonances is:

$$F(s) = \frac{M(s)}{1 - V(s)\Sigma(s)} = \left\{1 - g_1^2\left[a_1 + \Sigma(0)\right] - a_1\,\frac{m_1^2 g_1^2}{s - m_1^2} - \sum_{i=2}^{n} a_i\,\frac{s g_i^2}{s - m_i^2}\right\} \Bigg/ \left\{1 + \left(\frac{m_1^2 g_1^2}{s - m_1^2} + \sum_{i=2}^{n}\frac{s g_i^2}{s - m_i^2}\right)\frac{1}{2\pi}\left[k^2(s)\,\left\{h(m_1^2) - h(s)\right\} - k^2(m_1^2)\,h'(m_1^2)\,(m_1^2 - s) + \mathrm{i}\,\frac{k^3(s)}{\sqrt{s}}\right]\right\}. \tag{3.21}$$

3.4 Addition of Phase-Space and Centrifugal-Barriers Factors

Since we assumed in eq.(3.1) J^μ as source for the ρ, we have to imbed the form factor into the 3π decay. Therefore, we include the available phase space factors and the centrifugal barrier factors:

$$A(s) = N\,F(s)\,\overbrace{\frac{\sqrt{\lambda^{1/2}(s, m_\pi^2, m_\pi^2)\,\lambda^{1/2}(s, m_{3\pi}^2, m_\pi^2)}}{\sqrt{s}\,m_{3\pi}}}^{\text{phase-space factors}} \times \underbrace{\left[\frac{\lambda^{1/2}(s, m_\pi^2, m_\pi^2)}{\sqrt{s}}\right]^S \left[\frac{\lambda^{1/2}(m_{3\pi}, m_\pi^2, s)}{m_{3\pi}}\right]^L}_{\text{centrifugal-barrier factors}}, \tag{3.22}$$

with S being the orbital angular momentum in the 2π subsystem and L the orbital angular momentum between the 2π subsystem and the bachelor pion. N is a complex-valued normalization constant and λ is the Källén function:

$$\lambda(x, y, z) = x^2 + y^2 + z^2 - 2xy - 2yz - 2zx \tag{3.23}$$

In this work, we only consider the case where $L = 0$ and $S = 1$, therefore the final amplitude reads:

$$A(s) = N\,F(s)\,\frac{\lambda^{3/4}(s, m_\pi^2, m_\pi^2)\,\lambda^{1/4}(s, m_{3\pi}^2, m_\pi^2)}{s\,m_{3\pi}}, \tag{3.24}$$

where we used eqs.(3.21), (3.17), (3.9), (3.10) and (3.23).

3.5 Pole Parameters

In the complex s-plane this amplitude has one branch point starting at the 2π threshold, where $s = 4m_\pi^2$, because of the term $k(s)$ in eq. (3.17), which leads to a representation on two Riemann sheets. A resonance appears as a pole, which is defined with a flip of sign in contrast to a maximum, at s_{pole} in the so-called unphysical Riemann sheet. Due to analyticity, every pole requires an additional pole at s^*_{pole}. The pole with a negative imaginary part is closer to the physical Riemann sheet and thereby has more influence on the observables and is taken for the further analysis. This issue is shown in fig. 3.1. Taking the position s_{pole} of the pole, we can write a relation for the mass of the resonance m_{pole} and its width Γ_{pole} like in ref. [1]:

$$\sqrt{s_{\text{pole}}} = m_{\text{pole}} - \mathrm{i}\,\Gamma_{\text{pole}}/2 \tag{3.25}$$

The definition of the pole parameters in eq. 3.25 is not used consistently in the literature. Another definition for the pole parameters based on the Breit-Wigner amplitude reads

$$m^{\text{BW}}_{\text{pole}} = \sqrt{\text{Re}(s_{\text{pole}})} \quad \text{and} \quad \Gamma^{\text{BW}}_{\text{pole}} = -\frac{\text{Im}(s_{\text{pole}})}{\sqrt{\text{Re}(s_{\text{pole}})}}. \tag{3.26}$$

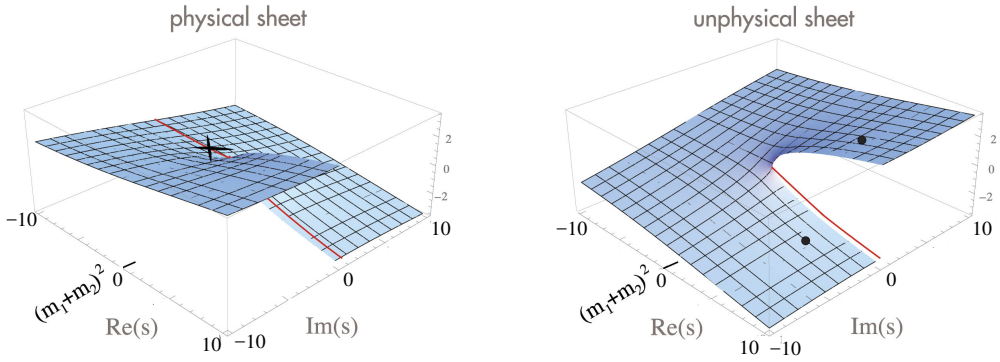

Figure 3.1: Sketch of the imaginary part of a typical amplitude in the complex s-plane. The dots mark possible resonance pole positions, the cross marks a bound state position. The picture is taken from [1].

Chapter 4

Fit Method

4.1 χ^2 Function for the Amplitude

To fit the theoretical model $\hat{\mathcal{T}}_i^{\text{bin}}$ in eq. (2.14), which includes the amplitude in eq. (3.24), to the measured data $\mathcal{T}_i^{\text{bin}}$, a χ^2 function is minimized. Because model and data are complex-valued the χ^2 function is formulated in terms of their real and imaginary parts.

$$\chi^2(\boldsymbol{\theta}, \mathscr{C}) = \sum_{\mathrm{j}=1}^{N_{\text{bins}}^{2\pi}} \frac{\left\{ \operatorname{Re}[\mathcal{T}_i^{\text{bin}}(m_{2\pi,j})] - \mathscr{C}\Delta_i^0 - \operatorname{Re}[\hat{\mathcal{T}}_i^{\text{bin}}(m_{2\pi,j}, \boldsymbol{\theta})] \right\}^2}{\sigma_{\text{Re},j}^2} + \frac{\left\{ \operatorname{Im}[\mathcal{T}_i^{\text{bin}}(m_{2\pi,j})] - \mathscr{C}\Delta_i^0 - \operatorname{Im}[\hat{\mathcal{T}}_i^{\text{bin}}(m_{2\pi,j}, \boldsymbol{\theta})] \right\}^2}{\sigma_{\text{Im},j}^2}. \tag{4.1}$$

Here, $\boldsymbol{\theta}$ represents the vector of fit parameters, $\mathscr{C}$ is the zero-mode coefficient, $N_{\text{bins}}^{2\pi}$ is the number of $m_{2\pi}$ bins, the higher index is the $m_{3\pi}$ bin, $\hat{\mathcal{T}}_i^{\text{bin}}$ is defined analogously to eq. 2.14:

$$\hat{\mathcal{T}}_i^{\text{bin}} = T_i \underbrace{A_i^{\text{bin}}}_{\alpha^{\text{bin}}}. \tag{4.2}$$

The value for t and $m_{3\pi}$ are constant, and every term is weighted by the inverse variances of the corresponding $\sigma_{\text{Re},j}^2$ and $\sigma_{\text{Im},j}^2$, respectively, so that data-points with high precision have more weight.
In order to take into account the statistical correlations between the data points we extend eq. 4.1 to

$$\chi^2(\boldsymbol{\theta}, \mathscr{C}) = \sum_j \sum_k \left[\mathcal{T}_i^{\text{bin}}(m_{2\pi,j}) - \mathscr{C}\Delta_i^0 - \hat{\mathcal{T}}_i^{\text{bin}}(x_{2\pi,j}, \boldsymbol{\theta}) \right] V_{jk}^{-1} \left[\mathcal{T}_i^{\text{bin}}(m_{2\pi,k}) - \mathscr{C}\Delta_i^0 - \hat{\mathcal{T}}_i^{\text{bin}}(x_{2\pi,k}, \boldsymbol{\theta}) \right], \tag{4.3}$$

where V_{jk} is the covariance matrix of the measured data in the $m_{2\pi}$ bins j and k as obtained from PWA.

The sum over all $m_{3\pi}$ bins of the χ^2 functions is then fitted with the `Minuit` algorithm [12], which gives us 8 fit parameters:

$$m_1, g_1, \mathrm{Re}(m_2), \mathrm{Im}(m_2), g_2, \mathrm{Re}(m_3), \mathrm{Im}(m_3), g_3,$$

used in every 3π bin, and for each $m_{3\pi}$ bin 5 additional parameters:

$$\mathrm{Re}(N), \mathrm{Im}(N), a_1, a_2, a_3,$$

used only in this particular $m_{3\pi}$ bin. The zero-mode corrections are handled numerical as in [8].

4.2 Pole Parameter Fitting

The model amplitude is infinity at the pole parameters. The pole parameters are estimated by minimizing the inverse of the modulus squared (eq. (4.4)) of the amplitude with the `Minuit` algorithm. This works, since the inverse value of the pole corresponds to a null.

$$1/|A(s)|^2. \tag{4.4}$$

The result has to fulfill

$$\frac{1}{A(s-\epsilon)} = -\frac{1}{A(s+\epsilon)}, \tag{4.5}$$

where $\epsilon \ll 1$ is a constant, because the sign of the pole has to change, as described in sec. 3.5.

Chapter 5

Results

From the waveset used in the PWA, that is described in chapter 2, we choose to analyze the $\pi^+\pi^-$ P-wave amplitude in $J^{PC}_X M^\epsilon J^{PC}_\xi L = 1^{++}0^+1^{--}S$, because this wave has the highest intensity. Therefore, the uncertainties are dominated by systematical uncertainties, which are not studied in this work, and are hence not specified. We only use the data of the lowest t' bin with $0.100\,(\mathrm{GeV}/c)^2 < t' < 0.141\,(\mathrm{GeV}/c)^2$, due to the main focus on the $m_{2\pi}$ and $m_{3\pi}$ dependence of the amplitude. The analyzed $m_{3\pi}$ range is subdivided into 50 equidistant bins in the range from $0.5\,\mathrm{GeV}/c^2$ to $2.5\,\mathrm{GeV}/c^2$. In the plots that will be shown below, the red points are the data from the PWA, while the blue data points are zero mode corrected. The fit results are plotted in orange.

5.1 Fit of the $\rho(770)$

In a first study, we only fit the $\rho(770)$, which dominates the $\pi^+\pi^-$ P-wave amplitude, in the limited $m_{2\pi}$ range below $1.2\,\mathrm{GeV}/c^2$. These data should contain only the ground state $\rho(770)$, since the nominal masses of the excited ρ states are well above $1.2\,\mathrm{GeV}/c^2$. Therefore, we fix all global parameters g_i and a_i in eq. 3.21, except m_1 and g_1, to zero. We get a large value of the fit quality $\chi^2/\mathrm{d.o.f.} = 10854/919 = 11.8$. This does not mean that the model is inapplicable, but that it describes not all the details of the high-precision data sufficiently. Since we have a large data set, the statistical uncertainty of the fit parameters is extremely small. For example, m_1 has a statistical uncertainty of 0.02%. In the future, systematical uncertainties have to be taken into account in order to obtain a final result for the quality of the fit.
For the $m_{3\pi}$ region, in which we obtained a peak in the $m_{3\pi}$ distribution (see fig. 1.3), the result is shown in fig. 5.1. We see that the real part of the amplitude is well described, but that the imaginary part of the model deviates from the data below $m_{2\pi} \approx 0.7\,\mathrm{GeV}/c^2$, which results mostly in a shift along the Argand diagram. Nevertheless, the general shape of the Argand diagram matches the data, which implies a passable fit of the model. Possible explanation of the deviation of the imaginary part of the amplitude could be that our model does not contain any

background terms, so that potential non-resonant components in the data cannot be described.

Fig. 5.2 shows a lower $m_{3\pi}$ mass bin. The Argand diagram matches not as good as in fig. 5.1. Again, the model deviates mostly in the low-mass region, this time particular in the real part.

For higher $m_{3\pi}$ bins, as e.g. shown in fig. 5.3, the description of the $\rho(770)$ is somewhat improved. The extrapolation of the model beyond the fit range of $m_{2\pi} = 1.2\,\mathrm{GeV}/c^2$ shows that a single resonance is not enough to describe the data.

The fitted parameters of $m_1 = 780.1\,\mathrm{MeV}/c^2$ and $g_1 = 4.524$ lead to a pole of the amplitude at $s = (0.5788 - 0.1158\mathrm{i})\,(\mathrm{GeV})^2$ (fig. 5.4), which corresponds to the $\rho(770)$ pole parameters of $m_{\mathrm{pole}} = 764.5\,\mathrm{MeV}/c^2$ and $\Gamma_{\mathrm{pole}} = 151.5.\,\mathrm{MeV}/c^2$.
Considering the definition based on the Breit-Wigner amplitude in eq. (3.26), we get the $\rho(770)$ pole parameters of $m^{\mathrm{BW}}_{\mathrm{pole}} = 760.7\,\mathrm{MeV}/c^2$ and $\Gamma^{\mathrm{BW}}_{\mathrm{pole}} = 152.2.\,\mathrm{MeV}/c^2$. Since the pole parameters should not be process dependent, we can compare to the values $m^{\mathrm{BW}}_{\mathrm{pole}} = (758.0 \pm 1.0)\,\mathrm{MeV}/c^2$ and $\Gamma^{\mathrm{BW}}_{\mathrm{pole}} = (145.2 \pm 1.2)\,\mathrm{MeV}/c^2$ extracted from the process $e^+e^- \to \pi^+\pi^-$ [13]. While our mass value is in agreement, we find a significantly larger width.

Now we study, whether the result changes, when we fit the full $m_{2\pi}$ range. The $\chi^2/\mathrm{d.o.f.} = 25921/1351 = 19.2$ increases, which can be explained by the fact that the model with only the $\rho(770)$ does not describe the high $m_{2\pi}$ region. For this fit we find $\rho(770)$ parameters of $m_1 = 780.2\,\mathrm{MeV}/c^2$ and $g_1 = 4.562$. Consequently, the $\rho(770)$ pole position is at $s = (0.5784 - 0.1168\mathrm{i})\,(\mathrm{GeV})^2$, i.e. the pole parameters $m_{\mathrm{pole}} = 760.5\,\mathrm{MeV}/c^2$ and $\Gamma_{\mathrm{pole}} = 170.9\,\mathrm{MeV}/c^2$. Since the fit parameters change only little, the quality of the description of the $\rho(770)$ in the data remains approximately the same.

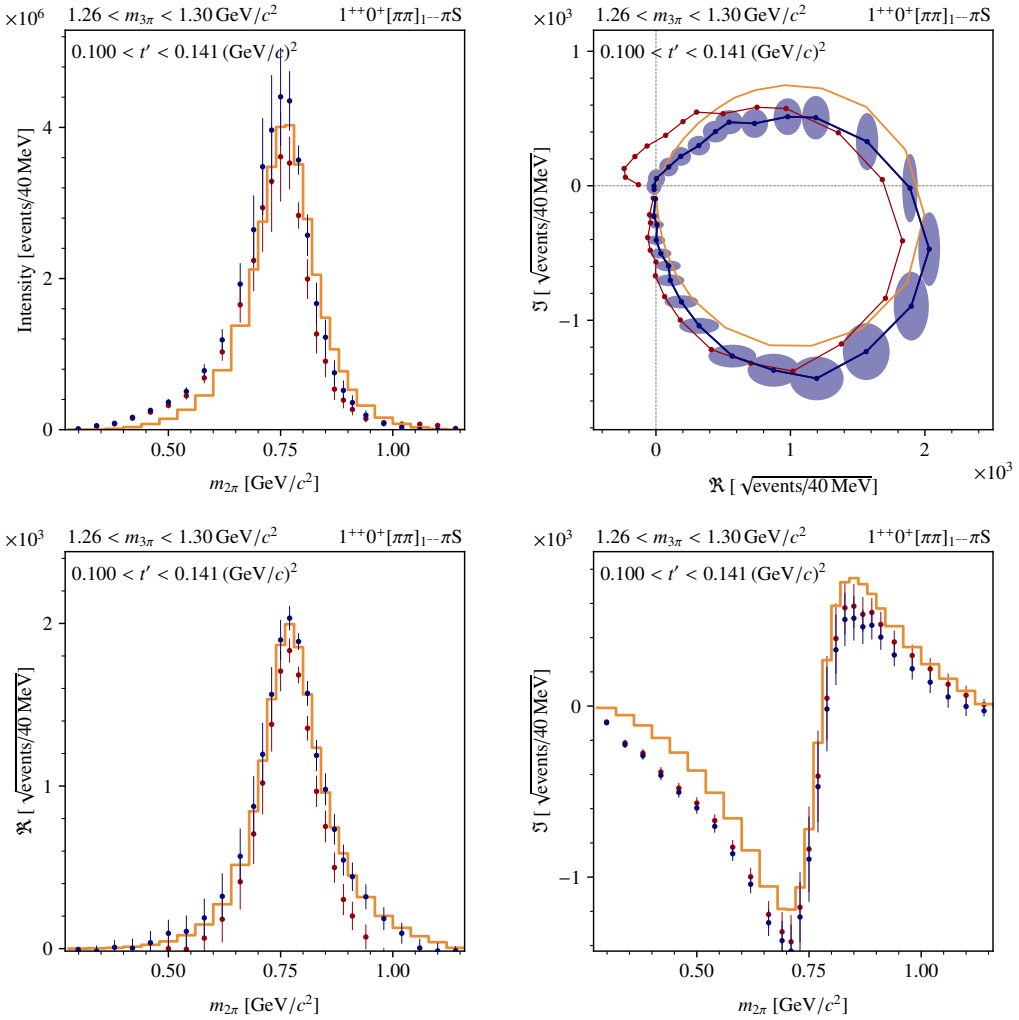

Figure 5.1: Intensity (top-left), Argand diagram (top-right), real (bottom-left) and imaginary (bottom-right) part of the $J^{PC}_X M^\epsilon J^{PC}_\xi L = 1^{++}0^+1^{--}S$ amplitude in the $m_{3\pi}$ bin $0.100\,(\mathrm{GeV}/c)^2 < m_{3\pi} < 0.141\,(\mathrm{GeV}/c)^2$. The red points are the data from the PWA and the blue points are the zero-mode corrected data. The model amplitude, which only contains the $\rho(770)$, is shown in orange.

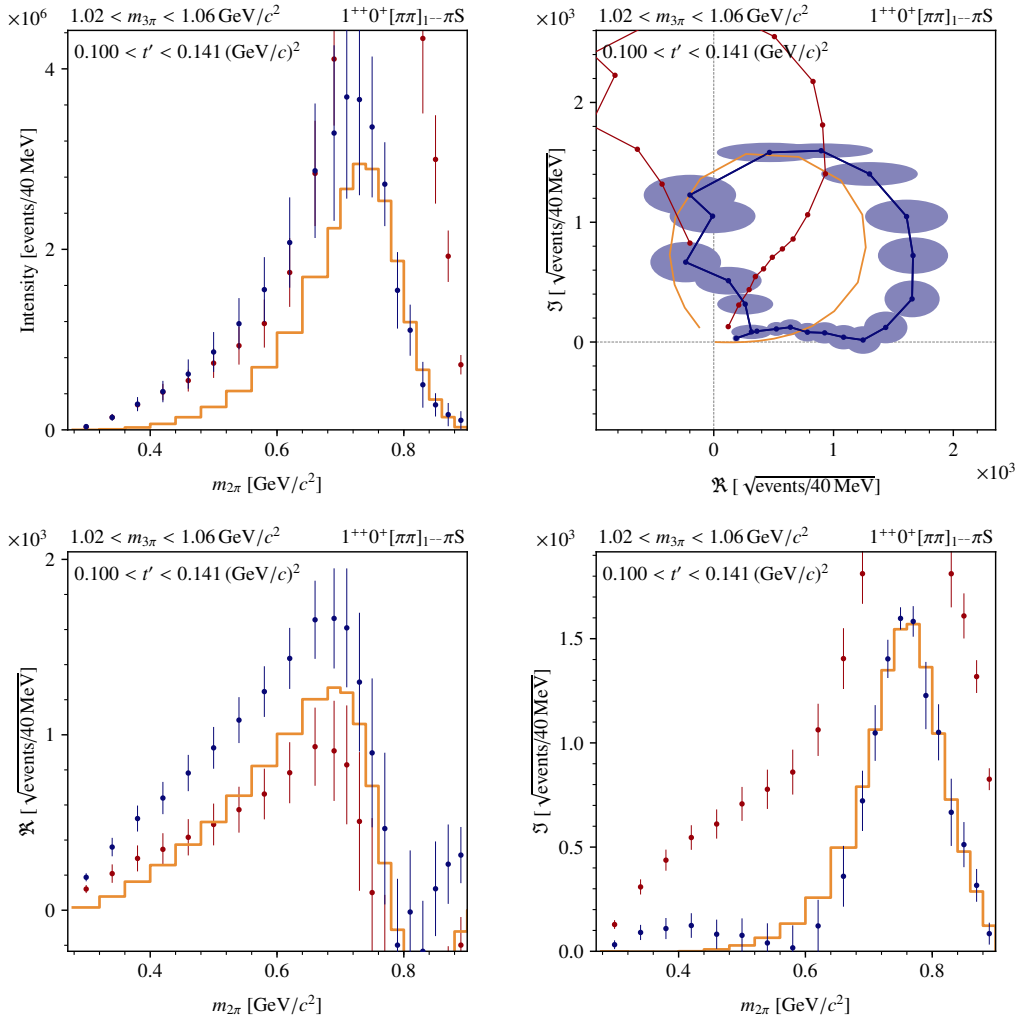

Figure 5.2: Similar to fig. 5.1, but showing a lower $m_{3\pi}$ bin.

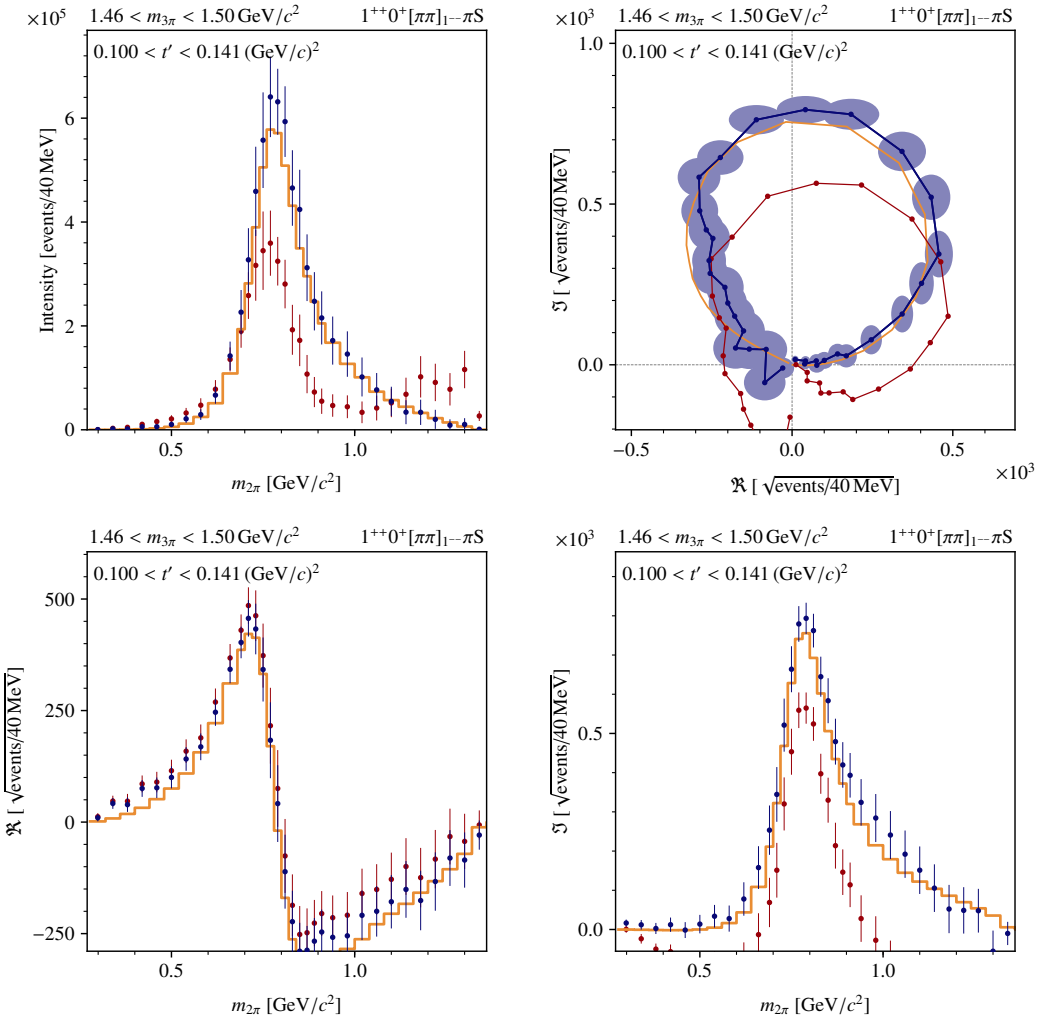

Figure 5.3: Similar to fig. 5.1, but showing a bin at large $m_{3\pi}$. Note that the $m_{2\pi}$ data above $1.2\,GeV/c^2$ were excluded from the fit.

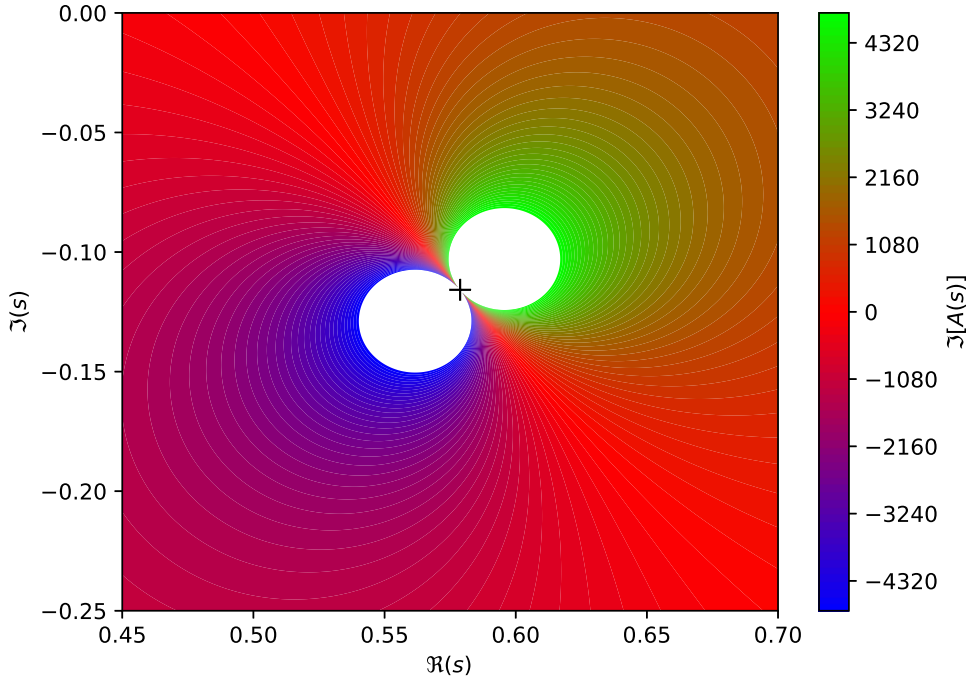

Figure 5.4: Plot of the imaginary part of the fitted amplitude in the complex s-plane. In the white areas $\mathrm{Im}[A(s)]$ is higher or lower than the scale, respectively. The position of the pole is indicated with the plus marker.

5.2 Fit of the $\rho(770)$ and the ρ'

Since our model in eq. 3.24 allows multiple resonances, we add an excited ρ resonance and fit the model in the whole $m_{2\pi}$ range. The fit quality of $\chi^2/\text{d.o.f.} = 20568/1298 = 15.8$, is better than for the fit with the model which contains only the $\rho(770)$. As expected, the fit describes the high-$m_{2\pi}$ better than the model without the ρ'. Also, the description of the $\rho(770)$ improves slightly (cf. e.g. figs. 5.1 and 5.5). The addition of higher ρ resonances influences the ground state and reduces the shift of the Argand diagram.

For higher $m_{3\pi}$ bins, e.g. fig. 5.6, the ρ' results in an additional loop in the Argand diagram, which matches better with the data. In this fit we see no separation of the ρ' and the ρ'' peak. Since we force the model to describe the higher $m_{2\pi}$ region with only one excited resonance, we get only an effective description, which shows up as a broad peak centered between the nominal masses of the $\rho(1450)$ and the $\rho(1700)$ at around $m_{2\pi} = 1.6\text{GeV}/c^2$.

The fit parameters are $m_1 = 777.7\,\text{MeV}/c^2$, $g_1 = 4.546$, $m_2 = (1.808 + 0.165\text{i})\,\text{MeV}/c^2$ and $g_2 = 3.227$. The amplitude has two resonance poles at $s_1 = (0.5763 - 0.1168\text{i})\,(\text{GeV})^2$, shown in fig. 5.7, and $s_2 = (2.445 - 0.5859\text{i})\,(\text{GeV})^2$ shown in fig. 5.8. The poles correspond to the $\rho(770)$ parameters of $m_{1,\text{pole}} = 763.0\,\text{MeV}/c^2$ and $\Gamma_{1,\text{pole}} = 153.1\,\text{MeV}/c^2$, and the ρ' parameters of $m_{2,\text{pole}} = 1574.7\,\text{MeV}/c^2$ and $\Gamma_{2,\text{pole}} = 372.1\,\text{MeV}/c^2$. The value of $m^{\text{BW}}_{1,\text{pole}} = 759.1\,\text{MeV}/c^2$ is closer to the value found in ref. [13], which supports our observation that the $\rho(770)$ is better described.

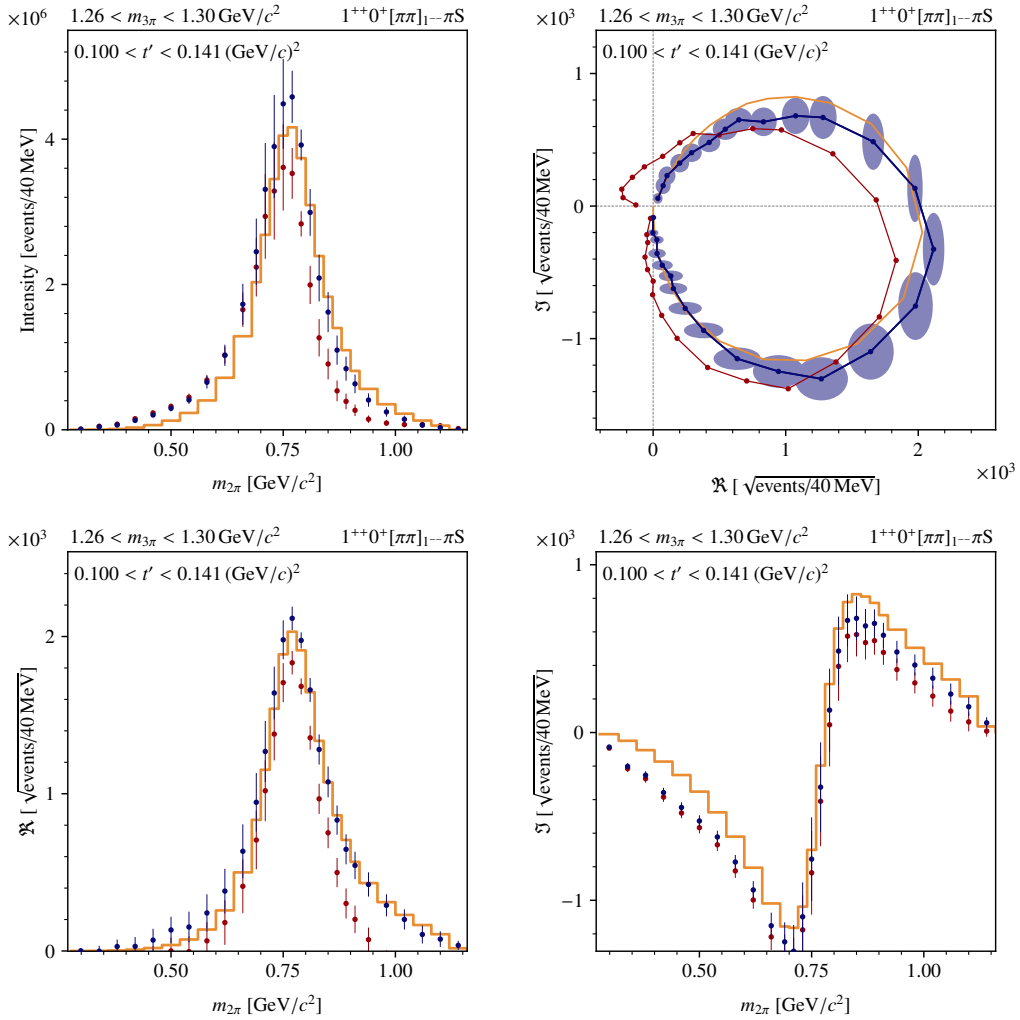

Figure 5.5: Similar to fig. 5.1, but showing the fit of a model containing $\rho(770)$ and ρ'.

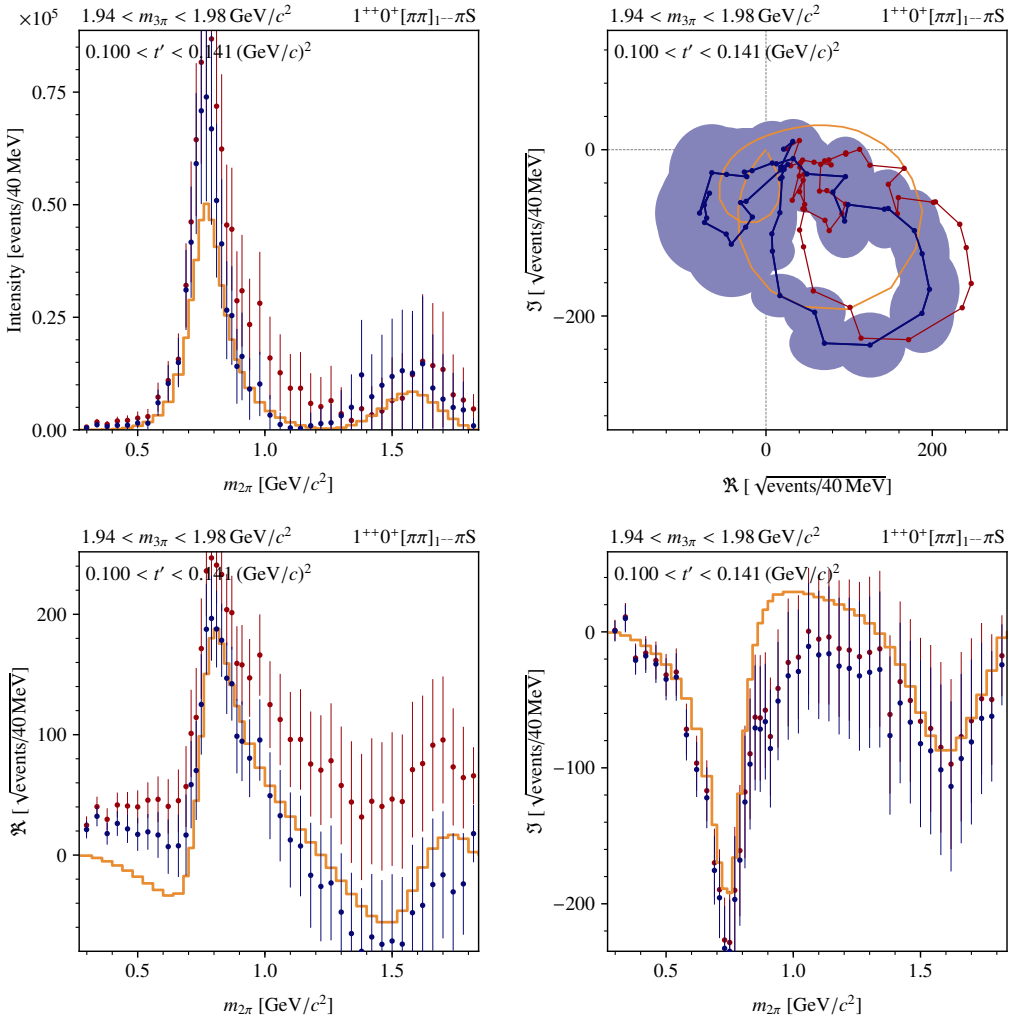

Figure 5.6: Similar to fig. 5.5, but showing a higher $m_{3\pi}$ bin.

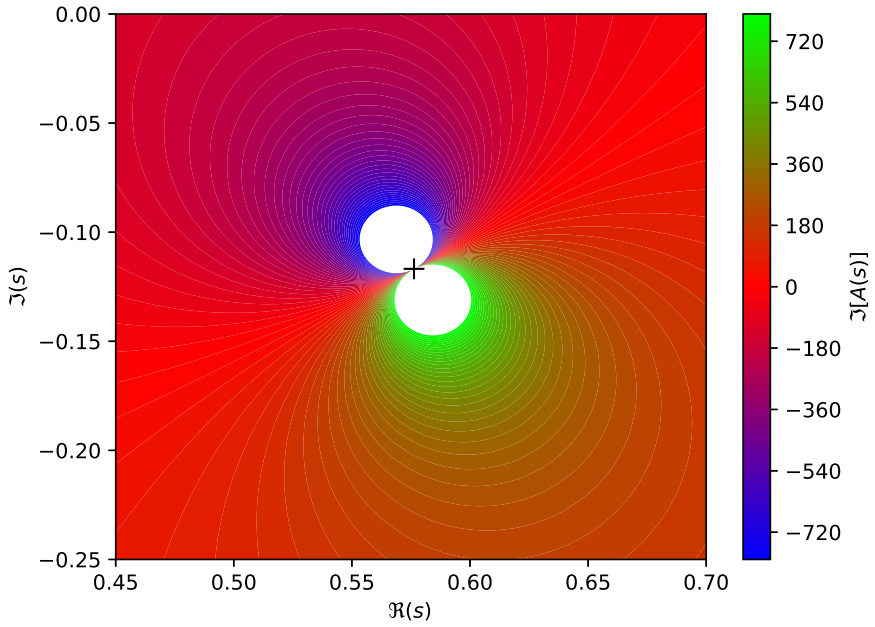

Figure 5.7: Similar to fig. 5.4, but showing the result for the fit of the $\rho(770)$ and the ρ'.

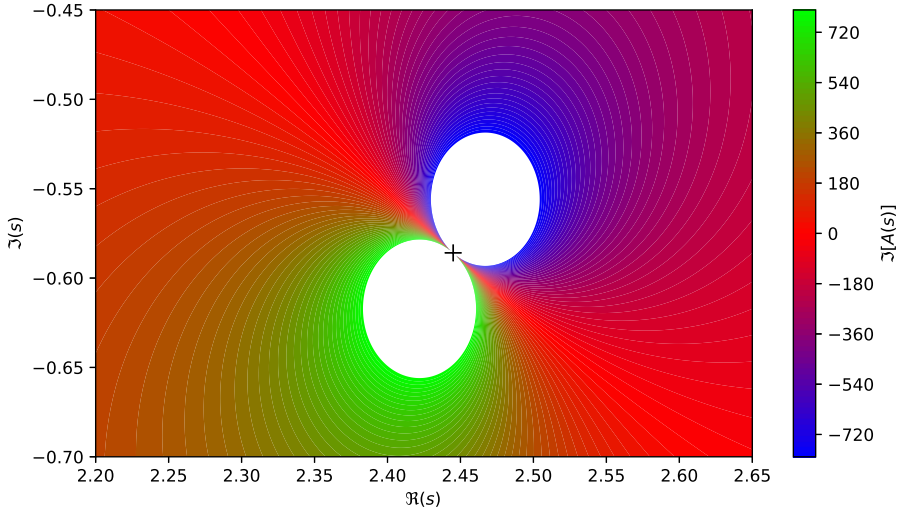

Figure 5.8: Similar to fig. 5.7, but showing the ρ' pole.

5.3 Fit of the $\rho(770)$, the ρ' and the ρ''

Since we know of three ρ-resonance in the available $m_{2\pi}$ range, we extend the model to three resonances. Attempts to fit all resonances simultaneously failed because the fit did not converge. So we fix the fit parameters of the $\rho(770)$ to the values found in sec. 5.2, where they were very likely already well determined, and fit only the ρ' and the ρ''. For this approach we get a fit quality of $\chi^2/\text{d.o.f.} = 14477/1245 = 11.6$, which is nearly half the value we got for the fit with only the $\rho(770)$ in the full $m_{2\pi}$ range. This means that our description of the high $m_{2\pi}$ region is good, since already the fit with $\rho(770)$ in the region $m_{2\pi} < 1.2\,GeV/c^2$ has a similar fit quality.
Fig. 5.10 shows the same $m_{3\pi}$ bin as fig. 5.6 for the fit of three resonances. We see that the description of the data in the high-$m_{2\pi}$ region and that of the shape of the Argand diagram is further improved. Since the zero-mode correction is also fitted and model dependent, the positions of the blue data points change. This leads to a peak centered around $1450\,\text{MeV}/c^2$, which is the nominal mass of the $\rho(1450)$. So it seems that we describe a clear excited ρ resonance.

In fig. 5.10, which shows an even higher $m_{3\pi}$ bin we see clearly two separated excited ρ resonances. The first peak is in the mass region of the $\rho(1450)$ and the second a bit above the $\rho(1700)$. In this $m_{3\pi}$ bin, the real and the imaginary part are fairly well described, which results in a matching shape of the Argand diagram. Since we fix the fit parameters of the $\rho(770)$, we only give the values of the other fit parameters. We obtain $m_2 = (1736 + 45.8\text{i})\,\text{MeV}/c^2$, $g_2 = 2.427$, $m_3 = (2560 + 589\text{i})\,\text{MeV}/c^2$, and $g_3 = 0.8006$. The pole positions are $s_2 = (2.539 - 0.5904\text{i})\,(\text{GeV})^2$ shown in fig. 5.11 and $s_3 = (6.116 + 2.576\text{i})\,(\text{GeV})^2$ shown in fig. 5.12. This corresponds to ρ' parameters of $m_{2,\text{pole}} = 1604\,\text{MeV}/c^2$ and $\Gamma_{2,\text{pole}} = 368.1\,\text{MeV}/c^2$, and to ρ'' parameters of $m_{3,\text{pole}} = 2525\,\text{MeV}/c^2$ and $\Gamma_{3,\text{pole}} = 1020\,\text{MeV}/c^2$. We obtain that the parameters of the ρ' have not change significantly compared to sec. 5.2. In ref. [14] the parameters of the Gounaris-Sakurai-amplitude are $m_{\rho'} = (1493 \pm 15)\,\text{MeV}/c^2$ and $\Gamma_{\rho'} = (427 \pm 31)\,\text{MeV}/c^2$ This supports rather our observation in sec. 5.2, that we have an effective description of the high-$m_{2\pi}$ region, than a description of the $\rho(1450)$. Comparing to $m_{\rho''} = (1861 \pm 17)\,\text{MeV}/c^2$ and $\Gamma_{\rho''} = (316 \pm 26)\,\text{MeV}/c^2$ found also in ref. [14], our result is extremely larger. Therefore, we remain only with a effective description of the high-$m_{2\pi}$ region.

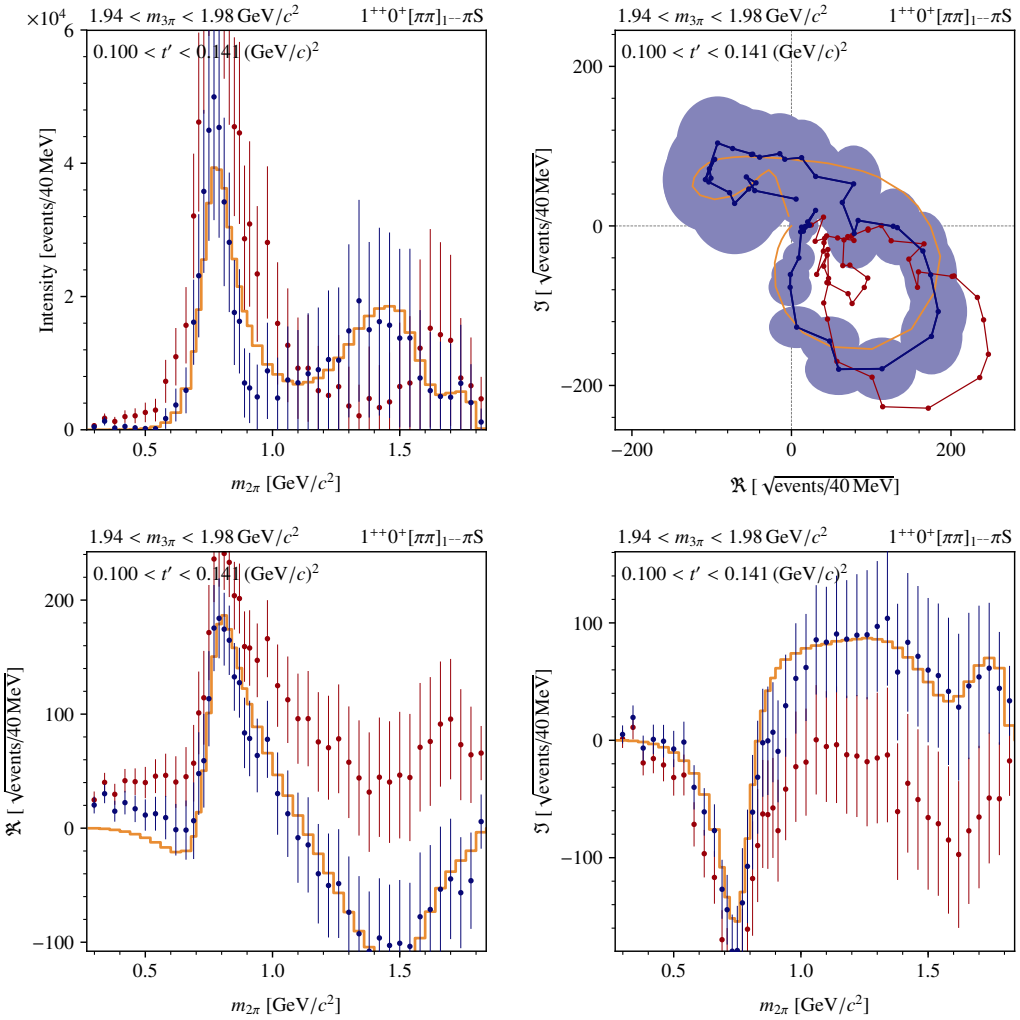

Figure 5.9: Similar to fig. 5.1, but showing the fit of a model containing the $\rho(770)$, ρ', and ρ'' in a high $m_{3\pi}$ bin.

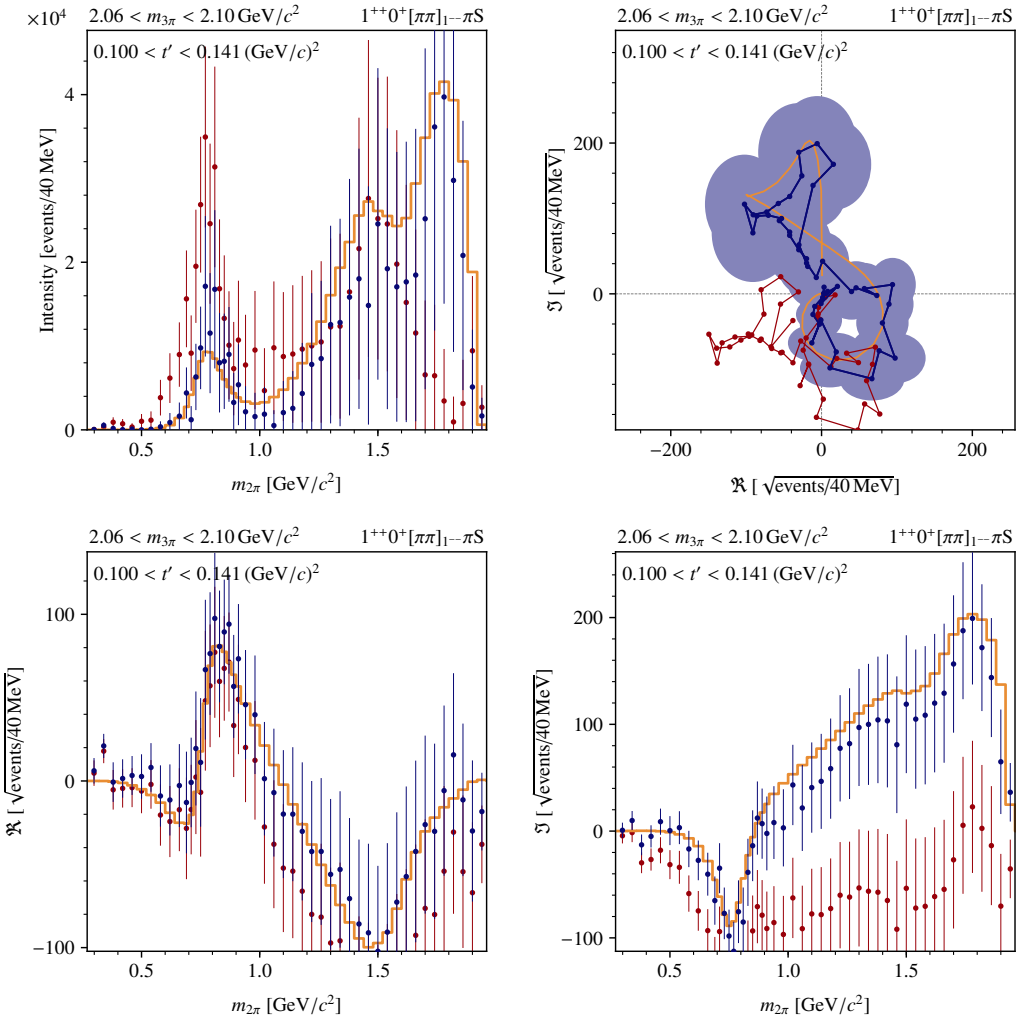

Figure 5.10: Similar to fig. 5.10, but showing a higher $m_{3\pi}$ bin.

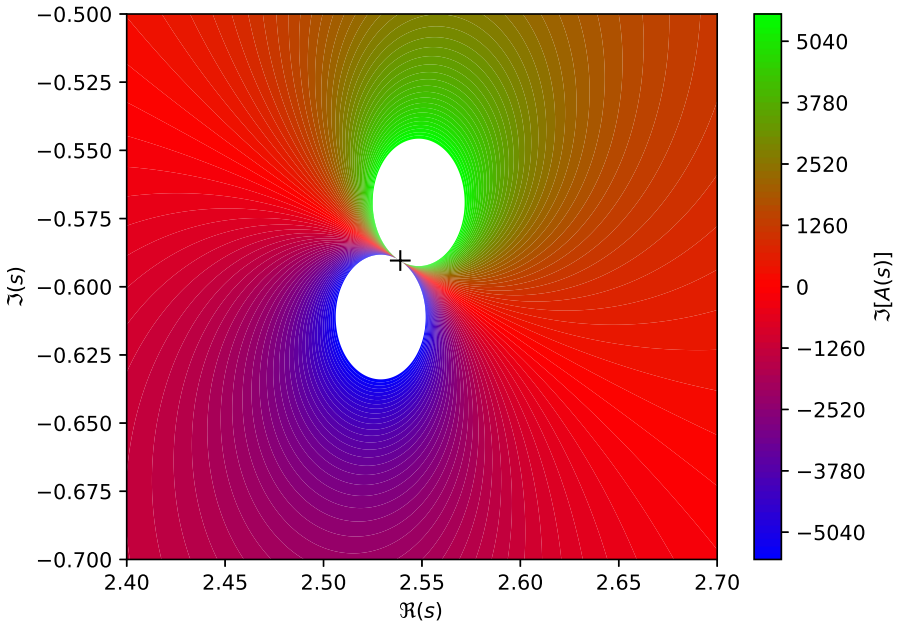

Figure 5.11: Similar to fig. 5.7, but showing the result for the fit of the $\rho(770)$, the ρ' and the ρ''.

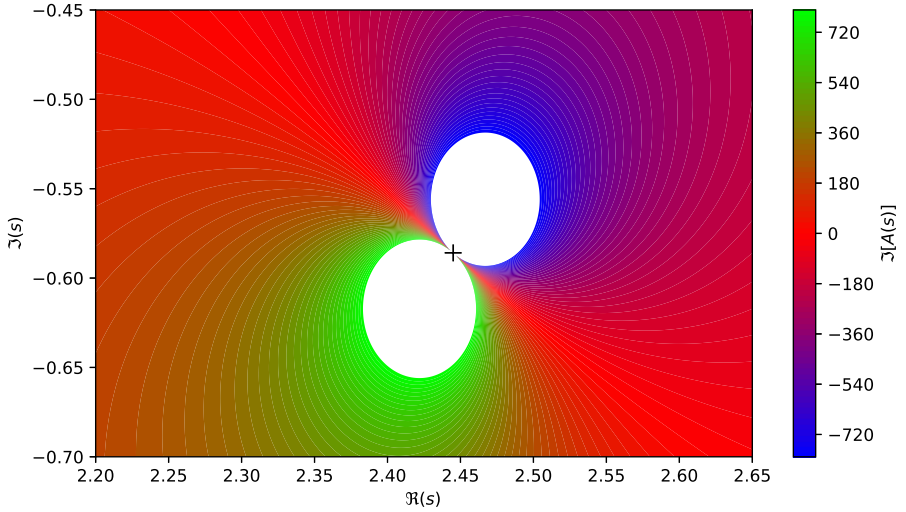

Figure 5.12: Similar to fig. 5.11, but showing the ρ'' pole.

Chapter 6

Summary and Outlook

6.1 Summary

In this work, we studied the $\pi^-\pi^+$ P-wave subsystem in $\pi^-\pi^-\pi^+$ events produced in inelastic $\pi^- p$ scattering reaction, which were measured by the COMPASS experiment at CERN. Based on a decomposition of the data into interfering quantum amplitudes with defined spin J and parity P quantum numbers of the 3π and the 2π system, we analyzed the $\pi^-\pi+$ P-wave amplitude for a 3π system with $J^P = 1^+$. Our goal was the description of the $\pi^-\pi+$ P-wave amplitude, in which the $\rho(770)$ is the ground state, in terms of resonances in the wave $J_X^{PC} M^\epsilon J_\xi^{PC} L = 1^{++}0^+1^{--}S$, based on the pion vector form factor derived in ref. [2]. Since this form factor describes the coupling to virtual photons, also ref. [2] added phase-space factors and barrier factors in order to account for the 3π environment. Because this amplitude is an analytic function in the complex s-plane, s being the square of the 2π mass, resonances appear as poles. The position of these poles in the s-plane are related to masses and widths of the resonance. For the fit itself we used a χ^2 function, taking into account the statistical correlation of the data points. In this method so-called zero modes ambiguities appear, which we resolved in our fit. We did four different fits. First, we fitted a model containing only the $\rho(770)$ while limiting $m_{2\pi}$ to be below $1.2\,\mathrm{GeV}/c^2$. We got a large value of the fit quality, while having small statistical uncertainties. We explained that the model is not inapplicable, but describes the data not in every detail, especially the low mass tail of the $\rho(770)$. We extracted the pole parameters and resulted with $m_{\mathrm{pole}} = 760.8\,\mathrm{MeV}/c^2$, which is in good agreement with the literature value, and $\Gamma_{\mathrm{pole}} = 152.2\,\mathrm{MeV}/c^2$, which is at least near the literature value. Then a second fit of the model in the whole available $m_{2\pi}$ range resulted in practically unchanged fit parameters, but a worsening of the fit quality due to the deviation of model and data at higher $m_{2\pi}$.
For our third fit we added an excited ρ resonance to the model. As expected, the fit quality at high $m_{2\pi}$ improved and also the description of the $\rho(770)$ got slightly better. The parameters of the excited ρ in the fit lie between the nominal masses of the $\rho(1450)$ and the $\rho(1700)$, so that we only got an effective description of the high-$m_{2\pi}$ region.

In the last fit, the model contained three resonances, while fixing the parameters of the $\rho(770)$, because otherwise the fit did not converge. In the result two separated peaks of the ρ' and the ρ'' were seen. This relatively good description of the higher $m_{2\pi}$ bins is also reflected in a fit quality value as good as for the first fit. But since the ρ' parameter of $m_{2,\text{pole}} = 1604\,\text{MeV}/c^2$ lies between the masses of the $\rho(1450)$ and the $\rho(1700)$ and the ρ'' parameter of $m_{3,\text{pole}} = 2525\,\text{MeV}/c^2$ is way above the nominal mass of the $\rho(1700)$, we get only an effective description of the high-$m_{2\pi}$ region.

6.2 Outlook

In this theses, we performed a proof-of-principal analysis in order to determine, whether the model from ref. [2] describes the COMPASS data in principle. Although we find that the model describes most of the data fairly well, there is still room for improvements in several aspects of the analysis. We could e.g. allow the parameters a_i to be complex-valued and check, whether this improves the fit quality. Maybe the most promising change could be the addition of non-resonant background terms, which seemed to be necessary in particular in the low-$m_{2\pi}$ regions. To reduce the statistical uncertainty in the high-$m_{2\pi}$ region, where we see signals of excited ρ resonances, we have the possibility to include the other three t' bins. At the same time we could study the dependence of the model parameters on t'. Since for the model with three ρ resonances the fit did not converge, when we let all parameters free, we could try to constrain the parameters into certain ranges. Another possibility to obtain a converged fit, could be a staged approach, in which we would try to fix different model parameter combinations in order to study the stability of the fit. To estimate the statistical uncertainties of the pole parameters, a resampling method could be used. Also, an estimation of systematic uncertainties is needed. There are also waves with other $J^{PC}_X M^\epsilon L$ quantum numbers that contain ρ resonances. For these waves a similar study would be interesting.
Finally, there are also resonances in other $\pi\pi$-waves. E.g. an analysis of the $\pi^+\pi^-$ D-wave in the $2^{-+}0^+[\pi\pi]2^{++}\pi S$ wave could study the dominant ground state $f_2(1270)$ and f_2 excited states.

Bibliography

[1] M. Tanabashi et al. 'Review of Particle Physics'. In: *Phys. Rev. D* 98 (3 2018), p. 030001. DOI: 10.1103/PhysRevD.98.030001.

[2] Lukas Bayer. 'Consistent extraction of ρ-parameters from various reactions'. Bachelor's Thesis. Rheinischen Friedrich-Wilhelms-Universität Bonn, Mar. 2019.

[3] P. Abbon et al. 'The COMPASS setup for physics with hadron beams'. In: *Nuclear Instruments and Methods in Physics Research A* 779 (2015), pp. 69–115. DOI: 10.1016/j.nima.2015.01.035. arXiv: 1410.1797 [physics.ins-det].

[4] P. Abbon et al. 'The COMPASS experiment at CERN'. In: *Nuclear Instruments and Methods in Physics Research Section A: Accelerators, Spectrometers, Detectors and Associated Equipment* 577.3 (2007), pp. 455–518. DOI: 10.1016/j.nima.2007.03.026.

[5] Florian Haas. 'Two-Dimensional Partial-Wave Analysis of Exclusive 190 GeV $\pi^- p$ Scattering into the $\pi^-\pi^-\pi^+$ Final State at COMPASS (CERN)'. PhD thesis. Feb. 2014. URL: https://cds.cern.ch/record/1662589.

[6] C. Adolph et al. 'Resonance production and $\pi\pi$ S-wave in $\pi^- + p \to \pi^-\pi^-\pi^+ + p_{\text{recoil}}$ at 190 GeV/c'. In: *Phys. Rev. D* 95 (3 2017), p. 032004. DOI: 10.1103/PhysRevD.95.032004.

[7] S.M. Flatté. 'On the nature of 0+ mesons'. In: *Physics Letters B* 63.2 (1976), pp. 228–230. ISSN: 0370-2693. DOI: https://doi.org/10.1016/0370-2693(76)90655-9.

[8] Fabian Michael Krinner. 'Freed-Isobar Partial-Wave Analysis'. PhD thesis. Technische Universität München, Feb. 2018.

[9] F. Krinner et al. 'Ambiguities in model-independent partial-wave analysis'. In: *Phys. Rev. D* 97 (11 2018), p. 114008. DOI: 10.1103/PhysRevD.97.114008.

[10] Christian Schneider. 'Generalisation of the Gounaris-Sakurai Parametrisation to overlapping inelasticresonances Resonances'. Bachelorarbeit. Bonn, 2018. URL: http://juser.fz-juelich.de/record/861996.

[11] G. J. Gounaris and J. J. Sakurai. 'Finite width corrections to the vector meson dominance prediction for rho —> e+ e-'. In: *Phys. Rev. Lett.* 21 (1968), pp. 244–247. DOI: 10.1103/PhysRevLett.21.244.

[12] F. James and M. Roos. 'Minuit – a system for function minimization and analysis of the parameter errors and correlations'. In: *Computer Physics Communications* 10 (1975). DOI: 10.1016/0010-4655(75)90039-9.

[13] M. Feuillat, J.L. Lucio M and J. Pestieau. 'Masses and widths of the $\rho^{\pm,0}(770)$'. In: *Physics Letters B* 501.1-2 (2001). DOI: 10.1016/s0370-2693(01)00104-6.

[14] J. P. Lees et al. 'Precise measurement of the $e^+e^- \to \pi^+\pi^-(\gamma)$ cross section with the initial-state radiation method at BABAR'. In: *Physical Review D* 86.3 (2012). DOI: 10.1103/physrevd.86.032013.